Surface-embedded Green-function method: A formulation using a linearized-augmented-plane-wave basis set

H. Ishida
College of Humanities and Sciences, Nihon University, Sakura-josui, Tokyo 156, Japan
(Received 28 November 2000; published 3 April 2001)

We present a first-principles method for calculating the Green function of a semi-infinite crystal surface using the embedding technique of Inglesfield and the linearized-augmented-plane-wave (LAPW) basis set. The calculation consists of two independent steps: (i) The embedding potential of a semi-infinite substrate is generated from the bulk crystalline potential, and (ii) a self-consistent surface Green function calculation is performed in the embedded surface region. The numerical advantages of our method over the previous ones are (i) that one does not need to determine the exact shape of the curvy embedding surface between the bulk and surface regions and (ii) that there is no need to explicitly treat the cap region (a portion of the muffin-tin sphere cut by a plane) of boundary atoms near the embedding surface. By virtue of them, the total amount of numerical work for performing a surface-embedded Green function calculation is reduced nearly to the same level as that in standard surface electronic-structure calculations within the slab approximation. As an example, we calculate the electronic structure of the (001) and (111) surfaces of Rh, Pd, and Ag.

DOI: 10.1103/PhysRevB.63.165409 PACS number(s): 73.20.At, 71.15.−m, 71.15.Mb

I. INTRODUCTION

Methods for calculating the electronic structure of crystal surfaces are divided into two groups. In the first one, the surface is modeled by a thin slab consisting of ~10 atomic layers. Combined with Car-Parrinello–like iterative techniques,[1] the slab geometry has been utilized extensively for first-principles total energy calculations of solid surfaces. In the second group, the surface is treated as a semi-infinite system. As an advantage, the semi-infinite method can fully describe the three-dimensional electronic band structure in a bulk crystal, which is essential for treating scattering problems such as photoemission and for studying Fermi-surface properties such as surface resistivity. The semi-infinite methods are further classified into those computing electron wave functions[2–7] and those treating the surface Green function.[8–12] The Green-function approach is suitable for ground-state electronic-structure calculations, since the charge density can easily be calculated by performing a contour integral in the complex energy plane. Most of the surface Green-function methods are based on the Dyson equation, where the Green function of a bulk crystal is computed as an unperturbed system.[8–10] For systems with simplified one-dimensional or muffin-tin (MT) potentials, the Green function can be constructed directly from the solutions of the Schrödinger equation.[11] The embedding method of Inglesfield[12] is unique in its formulation. In his method, one considers a surface region with a finite thickness embedded between the semi-infinite substrate and the vacuum, and their effects on the surface are taken into consideration via complex potential energies acting on the embedding surfaces on the substrate and vacuum sides.

Recently we developed a surface-embedded Green-function code using a plane-wave-like basis set and the norm-conserving pseudopotential.[13] A possible extention of the method toward handling the $2p$-row elements and transition metals may be to represent ion cores by the ultrasoft pseudopotential of Vanderbilt.[14] Instead, in the present work, we adopt linearized-augmented-plane-wave (LAPW) basis functions.[15] The surface embedding method combined with the LAPW basis set was originally developed by Inglesfield and Benesh.[16] In that work, the surface region was treated with the full-potential LAPW (FLAPW) scheme, whereas the embedding potential of the substrate was generated using a standard layer Korringa-Kohn-Rostoker (LKKR) technique within the MT potential approximation.[7] More recently Crampin *et al.* proposed a full-potential scheme for generating the embedding potential of a semi-infinite substrate within the embedding approach itself.[17] Their formulation was cast into a scattering theory and incarnated in an FLAPW-based surface Green-function code by van Hove.[18] In the present work, we aim at developing a computational method which enables us to perform a surface Green-function calculation at the same level of accuracy as that of van Hove[18] with significantly less numerical work.

The surface embedded Green-function calculation consists of two independent procedures. First, the embedding potential of a semi-infinite substrate is generated from the bulk crystalline potential. Second, a self-consistent electronic-structure calculation is performed in the surface embedded region. Our method has the following advantages in each step. Regarding the generation of the embedding potential, if the embedding surface on the substrate side is chosen as a plane, it intersects MT spheres of the boundary atoms. By adding the caps (a small portion of a MT sphere cut by the plane) of atoms on the surface side and removing those of atoms on the bulk side, one can define a surface embedded region that does not cut the MT spheres. The resultant embedding surface S_c, however, has a bumpy shape, which is numerically too complicated to treat. As was shown by Crampin *et al.*,[17] the embedding on S_c can be transmitted to embedding on an equivalent plane surface S, which is separated from S_c by a nonphysical buffer space Δ. In our method, the self-consistent equation for determining the embedding potential on S can be derived without specifying the

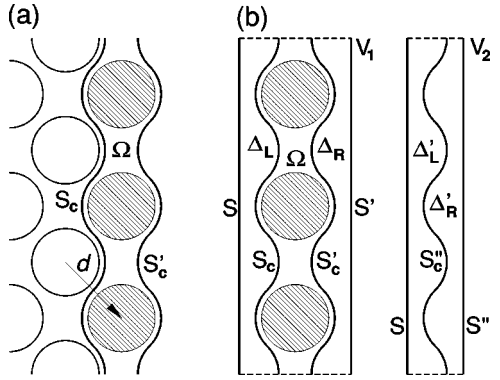

FIG. 1. Geometry for generating the embedding potential of a semi-infinite substrate. (a) Using a curvy embedding surface and (b) the present formulation.

exact shape of the original curvy surface S_c, and there is no need to separately calculate the contribution of the buffer space Δ to the overlap and Hamiltonian matrix elements. Also, in performing a self-consistent surface embedded calculation, we will avoid explicitly treating the caps of the boundary atoms. For example, with our method for calculating the Hartree potential, it is not necessary to evaluate partial multiple moments of the charge density in the cap region of the boundary atoms. As an application, numerical results are presented for the low-index surfaces of the last three $4d$ metals, Rh, Pd, and Ag.

The plan of the present paper is as follows. We describe the method for generating the embedding potential of a semi-infinite substrate in Sec. II and the method for performing a self-consistent Green-function calculation in the embedded surface region in Sec. III. Section IV contains results of the numerical calculation. A summary is given in Sec. V. Unless stated otherwise, we use the Hartree atomic units with $e=m=\hbar=1$ throughout this paper.

II. GENERATION OF THE EMBEDDING POTENTIAL

The idea behind the present method for generating the embedding potential of a semi-infinite substrate is similar to that in our previous work using pseudopotentials.[13] In the present work we treat an all-electron system and utilize the LAPW-like basis set instead of plane-wave-like basis functions. First, we outline the present formalism, focusing on our method for avoiding explicitly treating the cap region of the MT spheres. Regarding numerical details, in order to avoid repetition, we describe only those parts specific to the use of the LAPW basis functions. Let us consider a three-dimensional crystal with atomic layers piled up in the z direction [Fig. 1(a)]. Two adjacent lattice planes are related by a translational vector $\mathbf{d}=(\mathbf{d}_\parallel,d_z)$, where $\mathbf{d}_\parallel$ is in the xy plane.[19] We consider the Green function $G(\mathbf{r},\mathbf{r}')$ with energy ϵ in the half-space to the left of the embedding surface S_c, which is called a ''substrate.'' To avoid overlapping with the MT spheres of interface atoms, S_c is curved in a complex way.[20] G satisfies

$$[-\Delta/2+v_b(\mathbf{r})-\epsilon]G(\mathbf{r},\mathbf{r}')=-\delta(\mathbf{r}-\mathbf{r}'), \tag{1}$$

where v_b denotes the bulk crystalline potential. G is assumed to have zero normal derivative on S_c and to fulfill the outgoing (propagating or decaying toward the interior) boundary condition at $z=-\infty$. Using Green's theorem, one can show

$$\psi(\mathbf{r})=\frac{1}{2}\int_{S_c} d\mathbf{x}\, G(\mathbf{r},\mathbf{x})\frac{\partial\psi(\mathbf{x})}{\partial n}, \tag{2}$$

where $\mathbf{r}$ is an arbitrary point in the substrate, $\mathbf{x}$ is on S_c, n is the surface normal inward to the substrate, and ψ is a solution of the Schrödinger equation with energy ϵ subject to the outgoing boundary condition at $z=-\infty$. The embedding potential is defined by the inverse of G over S_c.[12] By setting $\mathbf{r}$ in Eq. (2) on S_c, one has

$$\frac{\partial\psi(\mathbf{x})}{\partial n}=2\int_{S_c} d\mathbf{x}'\, G_{S_c}^{-1}(\mathbf{x},\mathbf{x}')\psi(\mathbf{x}'), \tag{3}$$

which implies that the embedding potential $G_{S_c}^{-1}$ provides generalized logarithmic derivative of ψ on S_c. Now, we add one more atomic layer on top of the substrate and define a new embedding surface S_c'. Because of translational symmetry, the embedding potential on S_c', $G_{S_c'}^{-1}$, satisfies

$$G_{S_c}^{-1}(\mathbf{x},\mathbf{x}')=G_{S_c'}^{-1}(\mathbf{x}+\mathbf{d},\mathbf{x}'+\mathbf{d}). \tag{4}$$

By definition, $G_{S_c'}^{-1}$ is the surface-inverse of the Green function with zero normal derivative on S_c' and subject to the outgoing boundary condition at $z=-\infty$. However, the boundary condition at $z=-\infty$ can be replaced by Eq. (3) on S_c. Thus, it is possible to concentrate on volume Ω with a finite thickness in order to evaluate $G_{S_c'}^{-1}$. Crampin *et al.*[17] pointed out that Eq. (4) can be utilized as a self-consistent equation for determining the embedding potential itself:[17] Given an input $G_{S_c}^{-1}$, one calculates the Green function in Ω that satisfies the boundary condition imposed by Eq. (3) on S_c and has vanishing normal derivative on S_c'. Then, $G_{S_c'}^{-1}$ is determined as the inverse of G over S_c'. The left-hand side of Eq. (4) provides the output embedding potential $G_{S_c}^{-1}$, which should coincide with the input one.

The scheme described above is not suitable for a practical calculation because treating the curvy surfaces, S_c and S_c', is too complicated. In our formulation we set up two systems [Fig. 1(b)]. In region V_1, we add a buffer volume Δ_L to the left of S_c and Δ_R to the right of S_c'. In principle, the potential energy in Δ_L and Δ_R can be chosen arbitrarily. It will be specified later such that numerical work may be minimized. The second system V_2 is made by removing Ω from V_1 and displacing Δ_R by $-\mathbf{d}$. We simulate embedding on S_c by the embedding potential on an equivalent planar surface S, G_S^{-1}.[21] In order to obtain a self-consistent equation for determining G_S^{-1}, we begin with a trial embedding potential on S'', $G_{S''}^{-1}$. Given the boundary condition $G_{S''}^{-1}$, we integrate the Schrödinger equation from S'' through V_2 to obtain the

\embedding potential on S, G_S^{-1}. In the actual calculation, we use the embedding technique to calculate the Green function in V_2 that satisfies the boundary condition $G_{S''}^{-1}$ on S'' and has zero normal derivative on S. The embedding potential on S, G_S^{-1}, is given by the inverse of G over S. Next, we take the same G_S^{-1} as input and integrate the Schrödinger equation from S through V_1 to yield the embedding potential on S', $G_{S'}^{-1}$. The self-consistent condition for the correct embedding potential is given by $G_{S''}^{-1}=G_{S'}^{-1}$. This condition is equivalent to $G_{S_c''}^{-1}=G_{S_c'}^{-1}$ because the potential is the same in Δ_R and Δ_R'. Furthermore, $G_{S_c''}^{-1}=G_{S_c}^{-1}$, since we use the same G_S^{-1} to integrate the Schrödinger equation from S to S_c (S_c'') through Δ_L (Δ_L'). Thus, the original equation (4), $G_{S_c}^{-1}=G_{S_c'}^{-1}$, is reproduced.

Now, we specify the potential energy in Δ_L and Δ_R. If we utilize the original bulk crystalline potential v_b in these buffer volumes, the potential connects smoothly across S_c and S_c'. On the other hand, the MT spheres of the adjacent atomic layers are partially contained in Δ_L and Δ_R. In the overlapped region, v_b is expanded with spherical harmonics and radial functions. This is inconvenient, since we like to expand the Green function in Δ_L and Δ_R using plane waves alone. Hence, we need a model potential v_m that coincides with v_b in the interstitial region and is smooth enough inside the MT spheres. Fortunately, such a potential energy is constructed in the bulk FLAPW calculation to be performed before the surface calculation. As for the exchange-correlation potential, one can utilize that corresponding to the plane-wave part of the charge density in the bulk calculation. Although this charge density has no physical meaning inside the MT spheres, the corresponding exchange-correlation potential can be calculated in the entire bulk unit cell. As proposed by Weinert,[22] the interstitial part of the Hartree potential is constructed in the bulk FLAPW calculation by replacing true atomic charge densities in the MT spheres by smooth pseudocharge densities. The resultant Hartree potential is expanded in the entire bulk unit cell with plane waves, and thus, suitable for the Hartree part of the model potential v_m. With the above definition of v_m, the potential energy becomes smooth in the entire interstitial volume V_1-V_{MT} (V_{MT} denotes the volume corresponding to all the MT spheres contained in Ω). By virtue of this, the potential matrix element in V_1-V_{MT} can be calculated simultaneously without summing up each contribution from Δ_L, Δ_R, and the interstitial region of Ω separately. This signifies that there is no need to specify the actual shape of the true embedding surface S_c. One needs to specify only positions of the plane surfaces S and S'. S (S') can be located anywhere if the distance between S (S') and the atoms in volume Ω is larger than their MT radii. With our choice of v_m, the potential energy in region V_2 becomes also continuous across S_c'' because v_m has the translational symmetry of the bulk crystal. Thus, v_m is smooth in the entire volume of V_2.

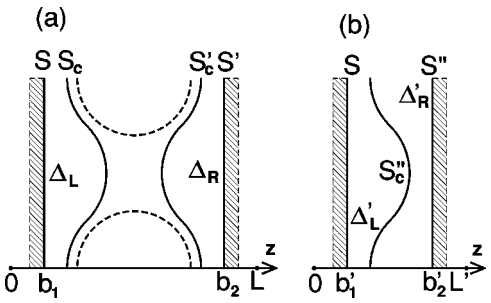

FIG. 2. Geometry and embedding parameters for generating the embedding potential of a semi-infinite substrate. (a) Region V_1 and (b) region V_2.

In the following, we describe some more numerical details. The Green function with energy ϵ and the two-dimensional wave vector $\mathbf{k}$ can be expanded as

$$G(\mathbf{r},\mathbf{r}')=\frac{1}{A}\sum_{\mathbf{g},\mathbf{g}'}\exp[i(\mathbf{k}+\mathbf{g})\cdot\mathbf{x}-i(\mathbf{k}+\mathbf{g}')\cdot\mathbf{x}']G(\mathbf{g}z,\mathbf{g}'z'), \tag{5}$$

where $\mathbf{r}=(\mathbf{x},z)$, A is the surface area, and $\mathbf{g}$ and $\mathbf{g}'$ are two-dimensional reciprocal lattice vectors corresponding to the Bravais lattice in the atomic plane. Similarly the embedding potential on the planar surface S is expanded as

$$G_S^{-1}(\mathbf{x},\mathbf{x}')=\frac{1}{A}\sum_{\mathbf{g},\mathbf{g}'}\exp[i(\mathbf{k}+\mathbf{g})\cdot\mathbf{x}-i(\mathbf{k}+\mathbf{g}')\cdot\mathbf{x}']G_S^{-1}(\mathbf{g},\mathbf{g}'). \tag{6}$$

In region V_1 we calculate the Green function with zero normal derivative on S' and subject to the boundary condition G_S^{-1} on S. The Green function is expanded with a non-orthogonal basis set $\{\chi_i\}$ as

$$G(\mathbf{r},\mathbf{r}')=\sum_{i,i'}G_{ii'}\chi_i(\mathbf{r})\chi_{i'}^*(\mathbf{r}'). \tag{7}$$

In the interstitial region V_1-V_{MT}, the basis function is

$$\chi_i(\mathbf{r})=\sqrt{\frac{2}{AL}}\exp[i(\mathbf{k}+\mathbf{g})\cdot\mathbf{x}]\sin(p_n z), \tag{8}$$

where $p_n=n\pi/L$ ($n\geqslant 1$) and i stands for a set of indices $(\mathbf{g},n)$. χ_i is used in a shorter interval $[b_1,b_2]$ instead of $[0,L]$ so that it can express the energy-dependent logarithmic derivative of electron wave functions on S and S' [see Fig. 2(a)]. Within the MT sphere of the α-th atom at $\mathbf{r}_\alpha$,

$$\chi_i(\mathbf{r})=\sum_{l,m}[A_{lm}u_l(r)+B_{lm}\dot{u}_l(r)]Y_{lm}(\mathbf{r}-\mathbf{r}_\alpha), \tag{9}$$

where $r=|\mathbf{r}-\mathbf{r}_\alpha|$, u_l is the radial solution of the scalar-relativistic Koelling-Harmon equation[23] at reference energy $\epsilon_{\alpha l}$, and $\dot{u}_l$ denotes its energy derivative. u_l has the large and small components and it is assumed that the small one vanishes at the MT radius $r=R_\alpha$. A_{lm} and B_{lm} are chosen such

that the large component of χ_i and its radial derivative connect continuously to the plane wave part (8) at $r=R_\alpha$.[15]

$G_{ii'}$ in Eq. (7) is calculated as $G_{ii'}=[\epsilon S-H]^{-1}_{ii'}$, where $S_{ii'}$ and $H_{ii'}$ are the overlap and Hamiltonian matrices, respectively. $H_{ii'}$ consists of three terms, i.e.,

$$H_{ii'}=t_{ii'}+v_{ii'}-(G_S^{-1})_{ii'}, \tag{10}$$

where the matrix element of the embedding potential, which is absent in standard slab calculations, is

$$(G_S^{-1})_{ii'}=\frac{2}{L}G_S^{-1}(\mathbf{g},\mathbf{g}')\sin(p_n b_1)\sin(p_{n'}b_1). \tag{11}$$

Regarding the free-electron part $t_{ii'}$, the contribution from the interstitial is $\frac{1}{2}\int_{V_1-V_{\rm MT}}d\mathbf{r}\,\nabla\chi_i^*(\mathbf{r})\cdot\nabla\chi_{i'}(\mathbf{r})$, while a standard scalar-relativistic treatment should be made inside the MT spheres.[15,23] Finally, the matrix element of the potential energy is calculated as

$$v_{ii'}=\int_{V_1-V_{\rm MT}}d\mathbf{r}\,\chi_i^*(\mathbf{r})v_m(\mathbf{r})\chi_{i'}(\mathbf{r}) + \int_{V_{\rm MT}}d\mathbf{r}\,\chi_i^*(\mathbf{r})v_b(\mathbf{r})\chi_{i'}(\mathbf{r}). \tag{12}$$

From $G_{ii'}$, we evaluate the Green function on S' ($z=b_2$). The embedding potential on S', $G_{S'}^{-1}(\mathbf{g},\mathbf{g}')$, is simply given by the inverse of the matrix $G(\mathbf{g}b_2,\mathbf{g}'b_2)$.

The calculation in region V_2 proceeds in a similar way. We employ a plane-wave-like basis set in the same form as Eq. (8). In the present case, $p_n=n\pi/L'$ ($n\geqslant 1$) and it is utilized in the interval $[b_1',b_2']$ [see Fig. 2(b)]. In V_2 no augmentation of the basis functions is necessary. We calculate the Green function with zero normal derivative on S ($z=b_1'$) and subject to the boundary condition $G_{S''}^{-1}$ on S'' ($z=b_2'$). The Hamiltonian matrix has three terms, i.e., $H_{ii'}=t_{ii'}+(v_m)_{ii'}+(G_{S''}^{-1})_{ii'}$. The last term has an opposite sign with the corresponding one in Eq. (10), since the surface normal n points toward the substrate ($n=-z$) in our definition, whereas, in the embedding Hamiltonian, one should use n outward from the embedded region ($n=z$). By the same reason, the output embedding potential on S ($z=b_1'$), $G_S^{-1}(\mathbf{g},\mathbf{g}')$, is given by the inverse of $-G(\mathbf{g}b_1',\mathbf{g}'b_1')$.

To reach self-consistency, we begin with some input $G_{S''}^{-1}$. In V_2, we calculate G_S^{-1}. Taking the same G_S^{-1} as input, we work in V_1 to calculate $G_{S'}^{-1}$. The self-consistent condition (4) is written in the present case as

$$G_{S''}^{-1}(\mathbf{g},\mathbf{g}')=\exp(i\mathbf{g}\cdot\mathbf{d}_\parallel)G_{S'}^{-1}(\mathbf{g},\mathbf{g}')\exp(-i\mathbf{g}'\cdot\mathbf{d}_\parallel). \tag{13}$$

The left-hand side of Eq. (13) is mixed with the original input $G_{S''}^{-1}$ to generate the next input potential on S''. We use a higher-dimensional Anderson method reformulated by Blügel[24] for the mixing procedure.

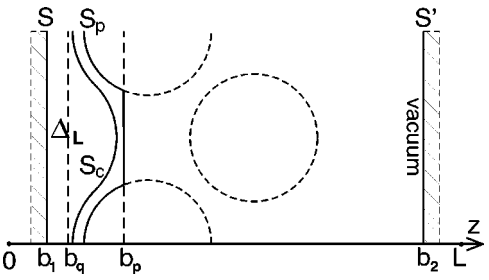

FIG. 3. Geometry and embedding parameters for a surface-embedded Green function calculation. The potential energy is determined self-consistently to the right of S_p.

III. SURFACE EMBEDDING CALCULATION

We perform a self-consistent Green-function calculation in the surface region embedded between the semi-infinite substrate and the vacuum. In accordance with the geometry in Sec. II, we introduce a planar embedding surface S ($z=b_1$) and a buffer volume Δ_L (Fig. 3). In Δ_L we use the smooth model potential v_m. The Green function is expanded by a nonorthogonal basis set in the same form as Eqs. (8) and (9). In the present case, the embedding potential on S' ($z=b_2$) expresses the effects of the semi-infinite vacuum. The embedding potential on S' is given as

$$G_{S'}^{-1}(\mathbf{g},\mathbf{g}')=-\frac{i}{2}\delta_{\mathbf{g}\mathbf{g}'}\sqrt{2(\epsilon-\epsilon_v)-|\mathbf{k}+\mathbf{g}|^2}, \tag{14}$$

where ϵ_v denotes the vacuum level, which should be determined self-consistently. The surface Green function is calculated as $G_{ii'}=[\epsilon S-H]^{-1}_{ii'}$, where

$$H_{ii'}=t_{ii'}+v_{ii'}-(G_S^{-1})_{ii'}+(G_{S'}^{-1})_{ii'}, \tag{15}$$

$$(G_{S'}^{-1})_{ii'}=\frac{2}{L}G_{S'}^{-1}(\mathbf{g},\mathbf{g}')\sin(p_n b_2)\sin(p_{n'}b_2). \tag{16}$$

The first three terms in Eq. (15) have the same form as the corresponding ones in Eq. (10). From the Green function, the output charge density is calculated as

$$n(\mathbf{r})=\frac{-2}{\pi}\,\mathrm{Im}\int^{\epsilon_F}d\epsilon\int_{\rm SBZ}\frac{d\mathbf{k}}{(2\pi)^2}G(\epsilon,\mathbf{k},\mathbf{r},\mathbf{r}), \tag{17}$$

where we explicitly expressed the dependence of the Green function on ϵ and $\mathbf{k}$.[25] In Eq. (17) the summation over $\mathbf{k}$ is taken in the surface Brillouin zone (SBZ) and the energy integration is performed along a complex contour, $(\epsilon_0,0)\rightarrow(\epsilon_0,\Gamma)\rightarrow(\epsilon_F,\Gamma)\rightarrow(\epsilon_F,0)$, where ϵ_0 is below the bottom of the bulk bands, $\Gamma=1\sim2$ eV, and ϵ_F denotes the Fermi level, which should be imported from the preceding bulk calculation in case of metallic systems. With the present basis set, the charge densities in the interstitial region and inside the MT sphere of the αth atom are expanded, respectively, as

$$n(\mathbf{r})=\sum_{\mathbf{g},n}n(\mathbf{g},n)\exp(i\mathbf{g}\cdot\mathbf{x})\cos(p_n z), \tag{18}$$

$$n(\mathbf{r})=\sum_{\nu} K_{\alpha\nu}(\mathbf{r}-\mathbf{r}_{\alpha})n_{\alpha\nu}(r), \tag{19}$$

where $p_n=n\pi/L$ $(n\geqslant 0)$ and $K_{\alpha\nu}$ are lattice harmonics of the α site. It is to be noted that Eq. (18) is physically meaningful only in the space between S_c and S'. The output charge density is mixed with the input one to generate the next input charge density. The iteration procedure is continued until the self-consistency in charge density is achieved.

Since the charge density given by Eqs. (18) and (19) has three-dimensional periodicity (the artificial lattice constant in the z direction is $2L$), one may use any method used in standard bulk calculations for evaluating the exchange-correlation potential v_{xc}. On the other hand, calculating the Hartree potential v_h is more complicated because of the boundary condition on the bulk side. In the first step, we replace the electron density (19) and the point nuclear charge in the MT spheres by a smooth model charge density using Weinert's method.[22] The resultant model charge density $\tilde{n}(\mathbf{r})$ can be expanded in the same form as Eq. (18). We introduce a plane $z=b_q$ slightly to the left of the true embedding surface S_c and consider the solution of the Poisson equation, $\Delta\tilde{w}(\mathbf{r})=-4\pi\tilde{n}(\mathbf{r})$, in the interval $[b_q,b_2]$. The solution for nonzero $\mathbf{g}$ components is

$$\begin{aligned}\tilde{w}(\mathbf{g},z)&=\frac{2}{|\mathbf{g}|}\int_{b_q}^{b_2}dz'\,\exp(-|\mathbf{g}||z-z'|)\sum_{n\geqslant 0}\tilde{n}(\mathbf{g},n)\cos(p_n z')\\&=\sum_{n\geqslant 0}\frac{4\pi\tilde{n}(\mathbf{g},n)}{p_n^2+|\mathbf{g}|^2}\cos(p_n z)+\tilde{w}_q\exp[-|\mathbf{g}|(z-b_q)]\\&\quad+\tilde{w}_2\exp[-|\mathbf{g}|(b_2-z)].\end{aligned} \tag{20}$$

For $\mathbf{g}=0$, it is possible to write the Hartree potential in the form,

$$\begin{aligned}\tilde{w}(\mathbf{g}=0,z)=\sum_{n\geqslant 1}\frac{4\pi}{p_n^2}[&\tilde{n}(\mathbf{g}=0,n)+c_q n_q(n)\\&+c_2 n_2(n)]\cos(p_n z),\end{aligned} \tag{21}$$

where $n_q(n)$ and $n_2(n)$ are the Fourier components of the model charge densities that are normalized to unity and localized in $[0,b_q]$ and $[b_2,L]$, respectively. The coefficients c_q and c_w are chosen such that $\tilde{w}$ satisfies the boundary condition $d\tilde{w}(\mathbf{g}=0,z)/dz=0$ at the vacuum $(z=b_2)$. The expressions for $\tilde{w}_q$, $\tilde{w}_2$, c_q, and c_2 as well as an example of the functional form of the model charge densities, $n_q(z)$ and $n_2(z)$, are given in Ref. 13.

The solution given above is not yet complete, since $\tilde{w}$ does not satisfy the correct boundary condition on the bulk side. Thus, as a correction, we add a solution of the Laplace equation, $\tilde{\phi}$, to $\tilde{w}$. $\tilde{\phi}$ is determined such that $\tilde{v}_h=\tilde{w}+\tilde{\phi}$ connects continuously to the bulk Hartree potential on the potential boundary surface to the bulk, S_p.[26] In the previous work using pseudopotentials,[13] we considered as S_p a plane surface $z=b_p$ located slightly on the surface side of S_c. Unfortunately, with the LAPW scheme, this plane cuts the MT spheres of atoms in the innermost surface layers as shown in Fig. 3. Thus, we need to introduce a new boundary surface S_p: If the plane $z=b_p$ intersects the MT sphere of a boundary surface atom, S_p is chosen as the cap surface of this MT sphere on the left-hand side of $z=b_p$, whereas S_p is chosen as the plane $z=b_p$ itself outside the MT spheres. The resultant S_p has a bumpy shape. But it is easy to determine $\tilde{\phi}$ as explained below.

First, we evaluate the bulk Hartree potential v_h minus $\tilde{w}$ on S_p as the boundary condition of $\tilde{\phi}$ on S_p. For $z\geqslant b_p$, $\tilde{\phi}$ can be written as

$$\tilde{\phi}(\mathbf{r})=\sum_{\mathbf{g}}\tilde{\phi}(\mathbf{g})\exp[-|\mathbf{g}|(z-b_p)]. \tag{22}$$

Diverging and linear terms are missing from Eq. (22) because they do not satisfy the boundary condition at the vacuum $z=b_2$. The coefficient $\tilde{\phi}(\mathbf{g})$ can be determined as the $\mathbf{g}$ component of $\tilde{\phi}(\mathbf{r})$ on the plane $z=b_p$. The value of $\tilde{\phi}(\mathbf{r})$ on $z=b_p$ is given as the boundary condition if $\mathbf{r}$ is located outside the MT spheres of boundary surface atoms, whereas it is not known when the plane $z=b_p$ is contained in the MT spheres. Thus, we adopt an iterative scheme and assume some input values for $\tilde{\phi}(\mathbf{g})$. Next, we consider the MT sphere of a boundary surface atom centered at $\mathbf{r}_\alpha$. Inside the sphere, $\tilde{\phi}$ can be expanded as

$$\tilde{\phi}(\mathbf{r})=\sum_{l,m}\tilde{\phi}_{lm}Y_{lm}(\mathbf{r}-\mathbf{r}_\alpha)\left(\frac{|\mathbf{r}-\mathbf{r}_\alpha|}{R_\alpha}\right)^l. \tag{23}$$

The coefficient $\tilde{\phi}_{lm}$ is determined as the (l,m) component of $\tilde{\phi}(\mathbf{r})$ on the MT surface. To the left of $z=b_p$, $\tilde{\phi}(\mathbf{r})$ on the sphere surface is known as it is a part of S_p. To the right of $z=b_p$, $\tilde{\phi}(\mathbf{r})$ can be evaluated using Eq. (22). Thus, it is possible to determine $\tilde{\phi}_{lm}$ from Eq. (22). Then, using Eq. (23), one evaluates $\tilde{\phi}(\mathbf{r})$ on the circular intersection of the MT sphere and the plane $z=b_p$. Since the value of $\tilde{\phi}(\mathbf{r})$ is now known on the entire surface of $z=b_p$, one can determine the output values of $\tilde{\phi}(\mathbf{g})$, which should be mixed with the input $\tilde{\phi}(\mathbf{g})$ until self-consistency is obtained.

So far, we have obtained the Hartree potential $\tilde{v}_h=\tilde{w}_h+\tilde{\phi}_h$ corresponding to the model charge density $\tilde{n}(\mathbf{r})$ in the volume to the right of S_p. The true Hartree potential v_h coincides with $\tilde{v}_h$ in the interstitial region. Inside the MT spheres, v_h can be calculated with the use of the same procedure as in a standard bulk FLAPW calculation: One integrates the Poisson equation on radial mesh points using the true MT charge density (19) such that it becomes continuous on the MT surface.[15] Finally, we comment on the calculation of the potential matrix element $v_{ii'}$ in Eq. (15) in the interstitial region. As the potential energy, we use the model potential v_m on the left-hand side of S_p and the self-consistent potential $v_s=v_{xc}+v_h$ on the right-hand side of S_p. Since S_p has a bumpy shape, if the two contributions are calculated separately, one must explicitly treat the cap region of the boundary atoms, which is numerically time consuming. To

avoid this, we employ the same real space technique as used in bulk FLAPW calculations.[15] Namely, we evaluate $v_s(\mathbf{r})\Theta(\mathbf{r})$ [$v_m(\mathbf{r})\Theta(\mathbf{r})$ on the substrate side of S_p] on the real space mesh points, where we choose $2L$ as an artificial period in the z direction and $\Theta(\mathbf{r})$ denotes a step function which equals unity in the interstitial region and zero inside the MT spheres. By performing a fast Fourier transform, the potential energy times the step function is expanded in the same form as Eq. (18). Using the basis functions of the form (8), the matrix element can be calculated very easily.

IV. RESULTS OF NUMERICAL CALCULATIONS

As a test of the present method, we perform a self-consistent electronic-structure calculation for the (001) and (111) clean surfaces of Rh, Pd, and Ag. All of them form an fcc lattice in the bulk. In the first step we calculate their bulk electronic structure at an experimental lattice constant using a standard bulk FLAPW code, from which we obtain the Fermi level ϵ_F and the bulk potential v_b. We also construct the smooth model potential v_m from v_b. Second, we generate the embedding potential of a semi-infinite metal for a given set of $\mathbf{k}$ points and energy mesh points following the procedure described in Sec. II. In the third step, we conduct a self-consistent surface-embedded Green-function calculation using the method described in Sec. III. In the present work we do not consider the relaxation of surface atomic layers, and the spacing between the neighboring lattice planes is set equal to the bulk value. In the calculation, two outermost lattice planes are included in the surface embedded region and the effects of the rest of the substrate are expressed by the embedding potential. For example, for Ag(001), the embedding parameters defined in Fig. 3 are chosen as $b_1=1.5$ a.u., $b_q=2$ a.u., $b_p=3.3$ a.u., $b_2=19$ a.u., and $L=20.5$ a.u. Regarding atomic parameters, the MT radius $R_s=2.64$ a.u., and the first and second lattice planes are located at $z=8.26$ and 4.42 a.u., respectively. The distance between $z=b_1$ and the second Ag layer, 2.92 a.u., is therefore slightly larger than R_s to allow for the space for the buffer volume Δ_L. In expanding the Green function inside the MT spheres, the maximum angular momentum for the basis functions (9) is $l_{\max}=9$, whereas the plane-wave cutoff energy for the basis functions in the interstitial is chosen as 10.2 Ry. We use the Ceperley-Alder[27] exchange-correlation potential within the local density approximation (LDA).

In Fig. 4 we show contour maps of the calculated charge densities on a vertical cut-plane containing atoms in the first layer and their nearest-neighbors in the second atomic layer for the (001) surfaces of Ag, Pd, and Rh. Figure 5 shows similar charge contour maps for their (111) surfaces. The thick dashed lines in these figures indicate positions of the potential boundary surface, S_p. On the surface side of S_p, we plot the self-consistent charge densities determined with the present surface-embedded Green-function method, whereas charge densities of the fcc crystals calculated with a bulk FLAPW code are plotted on the substrate side of S_p. It is seen that the charge density connects very smoothly across S_p, which signifies that our embedding potential simulates the effects of the semi-infinite crystal excellently. In the present calculational method, the Hartree potential v_h is constructed such that v_h becomes continuous across S_p. But we impose no boundary condition on the exchange-correlation potential v_{xc} on S_p. Thus, v_{xc} is discontinuous across S_p at the initial stage of the iteration procedure. Nevertheless, we see from Figs. 4 and 5 that the continuity of v_{xc} also holds well when the self-consistency in charge density is achieved. The charge-density maps of three metals look qualitatively very similar to one another for both the (001) and (111) surfaces. Looking more carefully, one notices that the charge density in the interstitial region decreases slightly with increasing atomic number reflecting a larger lattice constant and more localized d orbitals.

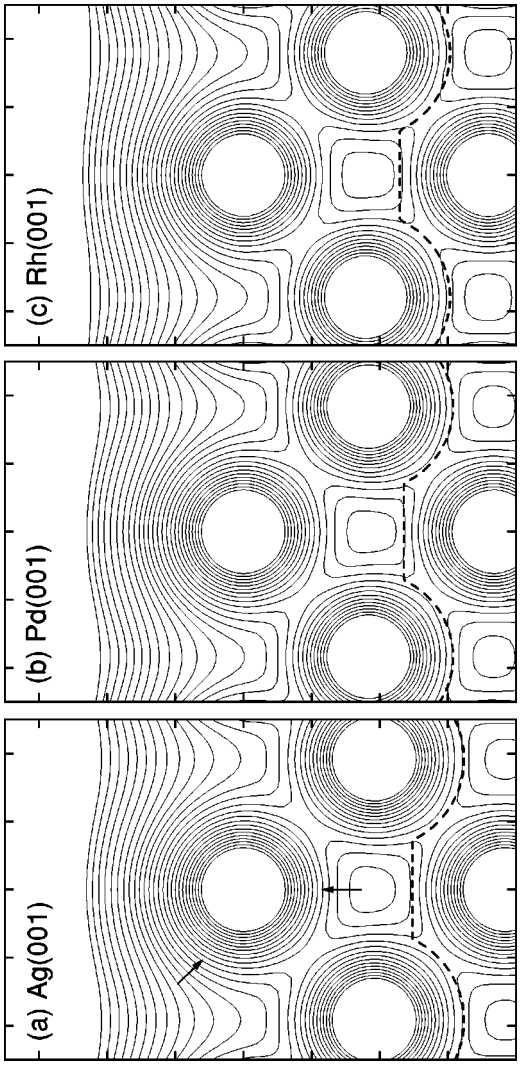

FIG. 4. Total charge density on a vertical cut plane containing atoms in the top layer and their nearest neighbors in the second layer for (a) Ag(001), (b) Pd(001), and (c) Rh(001). The lowest contour level is 5×10^{-4} a.u. and it increases successively by a factor of $10^{1/8}$. Arrows indicate directions toward which the charge density increases. Dashed lines indicate the crosscut of boundary surface S_p. The distance between neighboring ticks is 2 a.u.

The work function of a metal, Φ, can be calculated as the difference between the vacuum level and the Fermi energy, $\epsilon_v-\epsilon_F$. The calculated values of Φ are listed in Table I. For

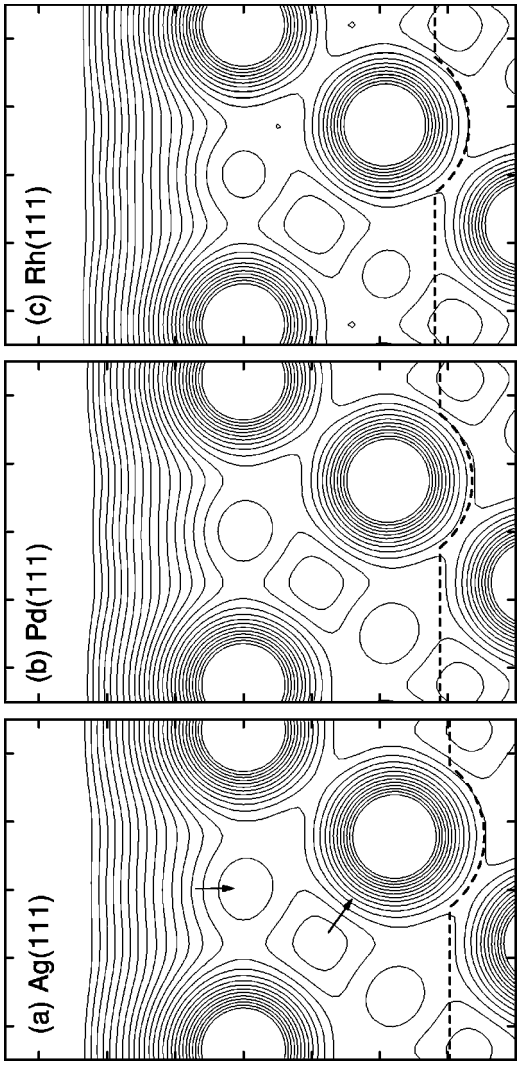

FIG. 5. As in Fig. 4, but for (a) Ag(111), (b) Pd(111), and (c) Rh(111) surfaces.

Ag(001), the previous slab-FLAPW calculations reported 4.74 eV[28] and 4.60 eV,[29] while the previous embedding calculations predicted $\Phi = 4.95$ eV[30] and 4.67 eV.[31] They scatter in a range of a few tenths of eV due to different numerical parameters. Also, different choice in the functional form of the exchange-correlation potential leads to a difference in Φ of ~ 0.1 eV. For Ag(111), our value 4.97 eV is in good agreement with 5.0 eV of Skriver and Rosengaard, who performed a comprehensive study of work functions for the fcc (111) and bcc (110) surfaces of all the $3d$, $4d$, and $5d$ metals using their Green-function technique based on the tight-binding linearized-muffin-tin-orbital (LMTO) method.[32] For Pd, the present results are in good agreement with the recent LDA values of Heinrichsmeier *et al.* calculated with a mixed-basis pseudopotential method within the slab approximation, i.e., 5.68 eV for Pd(001) and 5.75 eV for Pd(111).[33] They also calculated the work functions with a nonlocal exchange-correlation potential, which were, however, by ~ 0.4 eV larger than their LDA values. With the generalized gradient approximation (GGA), Pallassana *et al.*[34] predicted a smaller value, $\Phi = 5.42$ eV for Pd(111), which is in better agreement with recent measurements $\Phi = 5.44 \pm 0.03$ eV (Ref. 35) and 5.50 ± 0.01 eV.[36] Finally, our work function for Rh(111) is in fair agreement with 5.8 eV of Skriver and Rosengaard.[32] For an isolated Rh(001) monolayer, Wu and Freeman[29] obtained $\Phi = 5.77$ eV, which is fortuitously very close to our semi-infinite value.

TABLE I. Calculated work functions of Ag, Pd, and Rh(eV).

	Rh	Pd	Ag
(001)	5.74	5.73	4.80
(111)	5.72	5.74	4.97

One important advantage of the semi-infinite geometry is that it can describe localized surface states (SS) and surface resonances (SR) accurately. Especially, when an sp-like surface state appears near the edge of a projected bulk band gap, its wave function decays rather slowly toward the interior of the metal. It is difficult to treat such a SS with the standard slab approximation. Surface states on the (001) surfaces of noble and transition metals were previously studied by the embedding technique.[16,18,30] For Ag(001) we obtained a good agreement with the calculation of Aers and Inglesfield.[30] Hence, in the present paper, we show results for the (111) surfaces.

We define the **k**-resolved atomic density of states (DOS) by

$$\rho(\epsilon, \mathbf{k}) = -\frac{1}{\pi} \int d\mathbf{r}\, \mathrm{Im}\, G(\epsilon + i\delta, \mathbf{k}, \mathbf{r}, \mathbf{r}), \tag{24}$$

where the volume integral is done in a MT sphere and δ is an infinitesimal positive number. Solid lines in Fig. 6(a) show the calculated DOS of a top-layer atom for Ag(111) at four **k** points along the $\bar{\Gamma}$-$\bar{\mathrm{K}}$ line in SBZ.[37] Also shown by dashed lines is the contribution of the p $(l=1)$ orbitals to $\rho(\epsilon, \mathbf{k})$. In calculating the DOS, δ in Eq. (24) was replaced by a small positive number $\eta = 5 \times 10^{-4}$ a.u. in order to avoid the SS poles on the real energy axis. The width of SS peaks in this figure is therefore just an artifact of η. It is well known that the Ag(111) surface has a partially filled Shockley-type SS in the projected sp-band gap near the center of SBZ. Kevan and Gayloard[38] investigated this state by angle-resolved photoemission spectroscopy and obtained $E_0 = -0.12$ eV as its binding energy relative to ϵ_F at $\bar{\Gamma}$. In Fig. 6(a) the SS peak is located at -0.11 eV below ϵ_F at $\bar{\Gamma}$ in good accord with their experiment. This state is dominantly p-like in orbital character and has a parabolic energy dispersion at small **k**. The calculated effective mass $m^* = 0.37$ a.u. is smaller than $m^* = 0.53$ a.u. deduced from the inverse photoemission spectra.[38] We also see from Fig. 6(a) that the energy difference between the SS peak and the upper edge of the projected sp bulk band (indicated by vertical bars) decreases with increasing wave number. In the uppermost curve corresponding to $|\mathbf{k}| = 0.4$ a.u., the SS merges into the projected band and appears as a surface resonance. We emphasize that

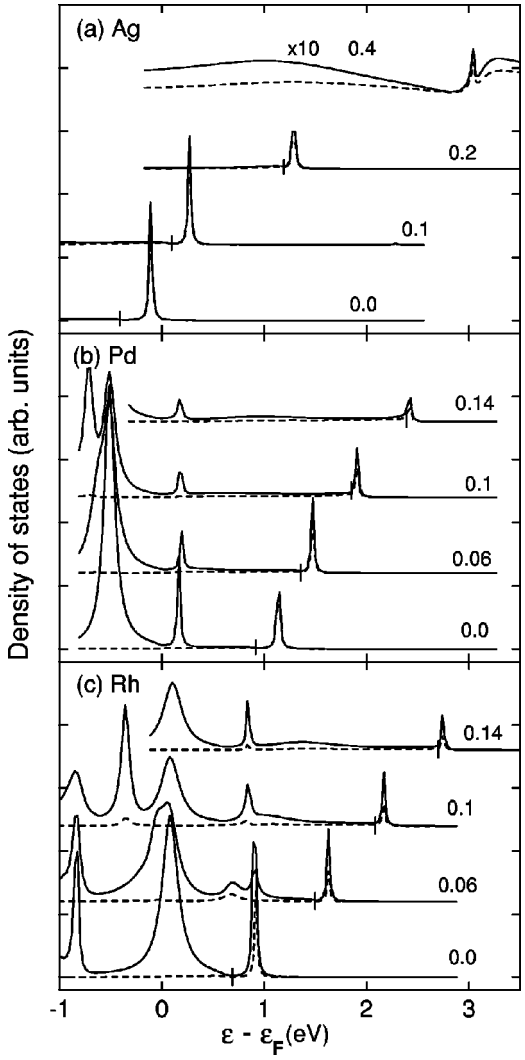

FIG. 6. Atomic density of states, $\rho(\epsilon,\mathbf{k})$, for top-layer surface atoms along $\bar{\Gamma}-\bar{\mathrm{K}}$ line in SBZ (solid lines). Dashed lines show the p component of $\rho(\epsilon,\mathbf{k})$. (a) Ag(111), (b) Pd(111), and (c) Rh(111). Small numbers near each line indicate the wave number $|\mathbf{k}|$ in atomic units. Vertical bars are the upper edge of the projected sp-bulk band. The imaginary part of energy $\eta=5\times10^{-4}$ a.u.

such a transition from a true SS to a SR is difficult to analyze with the standard slab approximation.

Figure 6(b) shows the top-layer atomic DOS for Pd(111). Very recently, energy positions and lifetimes of the unoccupied Schockley states and image-potential states on Pd(111) were studied by two-photon photoemission (2PPE) spectroscopy by Schäfer *et al.*[36] In order to calculate the image-potential states, one must replace the embedding potential (14) on the vacuum side by that corresponding to the image potential ($\propto -1/z$).[39] As the aim of the present calculation is just to test our new calculational scheme, instead of doing so, we focus on Schockley states in this work. Schäfer *et al.*[36] also analyzed measured lifetimes of the surface states using a one-dimensional model and the GW approximation. At present, it is too complicated to perform such a GW calculation using a fully three-dimensional Green function as obtained in the present work. On Pd(111), an unoccupied

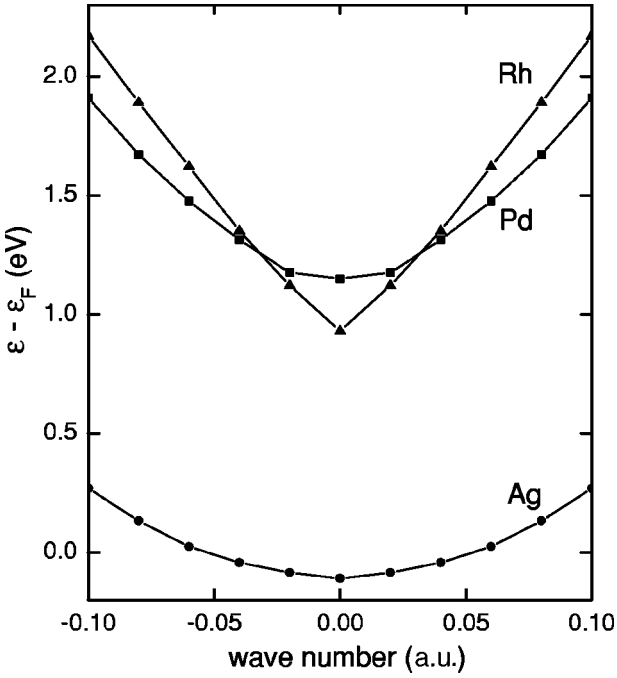

FIG. 7. Energy dispersion of the p-like surface state along $\bar{\Gamma}$-$\bar{\mathrm{K}}$ for the (111) surface of Ag, Pd, and Rh. Lines between symbols are guides for eyes.

Shockley-type surface band near the center of SBZ was predicted by Louie[40] and observed via inverse photoemission spectroscopy by Hulbert *et al.*[41] Its energy at $\bar{\Gamma}$ was found to be 1.3 eV above the Fermi level. More recent 2PPE experiments reported similar values, 1.26 ± 0.03 eV (Ref. 35) and 1.35 ± 0.02 eV.[36] In the present calculation, the corresponding Shockley state appears slightly at a lower position, i.e., at 1.15 eV above ϵ_F at $\bar{\Gamma}$. As in the case of Ag(111), this state has a strong p character and a parabolic energy dispersion. Its effective mass $m^*=0.18$ a.u. is in fair agreement with a recent theoretical value of Heinrichsmeier *et al.*, $m^*=0.22$, but is much smaller than that determined by inverse photoemission,[41] $m^*=0.35$ a.u. In Fig. 6(b) we find the second SS peak at 0.2 eV above ϵ_F at $\bar{\Gamma}$. This state, which is located slightly above the upper edge of the bulk $4d$ band (L_3), is twofold degenerate and predominantly made of d orbitals. Although it couples with projected bulk bands and becomes a SR except at $\bar{\Gamma}$, its interaction with them is relatively weak and it remains a noticeable peak along the $\bar{\Gamma}$-$\bar{\mathrm{K}}$ direction having a much smaller energy dispersion than the p-like SS. Hulbert *et al.*[41] observed a large peak immediately above the Fermi level in their inverse photoemission spectra from Pd(111) and assigned the peak as originating from the unoccupied d band. It may be likely that the peak corresponds to the d-like surface state.

We show in Fig. 6(c) the atomic DOS for the top-layer atom of Rh(111). As in the case of Pd(111), the p-like SS and d-like SS appear at $\bar{\Gamma}$ above ϵ_F. As the upper edge of the bulk $4d$ band (L_3) and that of the sp band ($\mathrm{L}_{2'}$) are close to each other for Rh, both are located at 0.9 eV above the Fermi level and we observe only a single large peak in

Fig. 6(c). The *d*-like state becomes broader with increasing **k** keeping its energy position nearly unchanged. By a self-consistent linear combination of atomic orbitals (LCAO) calculation, Feibelman[42] studied the electronic structure of an 11-layer Rh(111) slab and found a SS at ~ 1 eV above the Fermi level at the center of SBZ. The orbital character of this state was not mentioned in that work. In Fig. 7 we summarize the energy dispersion of the *p*-like surface state at small $|\mathbf{k}|$ along the $\bar{\Gamma}$-$\bar{\mathrm{K}}$ direction for the three metals. For Rh, its dispersion deviates from a quadratic behavior even at small $|\mathbf{k}|$ and is difficult to fit by a single effective mass.

Before closing this section, we comment on total energy. We are planning to implement subroutines to compute the total energy of the system with the embedding method. On the other hand, the total energy and atomic forces of solid surfaces can be calculated rather accurately even with a thin slab in most cases. Thus, a more practical way might be to optimize the atomic geometry with an existing slab code at first and to use that geometry in the subsequent semi-infinite Green-function calculation. This does not negate the importance of semi-infinite methods, since there are a wide variety of problems that can be studied only using truly semi-infinite geometry.

V. SUMMARY

We have presented a method for calculating the Green function of semi-infinite crystal surfaces using the LAPW basis set and the embedding approach of Inglesfield. The method comprises two independent steps: First, the embedding potential of a semi-infinite substrate is generated from the bulk crystalline potential. Second, a self-consistent surface Green-function calculation is performed in the embedded surface region. The great advantages of the present method over the previous ones are (i) that there is no need to specify the exact shape of the true embedding surface throughout the calculation, and (ii) that one does not need to treat separately the caps of the muffin-tin spheres of the boundary surface atoms. By virtue of them, the amount of numerical work for performing a self-consistent surface-embedded calculation can be reduced to the same level as that in a standard bulk FLAPW calculation. As a test, we performed a self-consistent electronic structure calculation for the (001) and (111) clean surfaces of Rh, Pd, and Ag. We have studied the charge density, work functions, and the surface states of these surfaces.

[1] R. Car and M. Parrinello, Phys. Rev. Lett. **55**, 2471 (1985).
[2] E. E. Krasovskii and W. Schattke, Phys. Rev. B **56**, 12 874 (1997); **59**, R15 609 (1999).
[3] W. Hummel and H. Bross, Phys. Rev. B **58**, 1620 (1998).
[4] K. Hirose and M. Tsukada, Phys. Rev. B **51**, 5278 (1995).
[5] M. D. Stiles and D. R. Hamman, Phys. Rev. B **38**, 2021 (1988).
[6] J. A. Appelbaum and D. R. Hamann, Phys. Rev. B **6**, 2166 (1972).
[7] J. B. Pendry, *Low Energy Electron Diffraction* (Academic, London, 1974).
[8] P. Krüger and J. Pollmann, Phys. Rev. B **38**, 10 578 (1988).
[9] H. L. Skriver and N. M. Rosengaard, Phys. Rev. B **43**, 9538 (1991).
[10] V. S. Stepanyuk, W. Hergert, K. Wildberger, R. Zeller, and P. H. Dederichs, Phys. Rev. B **53**, 2121 (1996).
[11] A. Liebsch, *Electronic Excitations at Metal Surfaces* (Plenum, New York, 1997), p. 40.
[12] J. E. Inglesfield, J. Phys. C **14**, 3795 (1981).
[13] H. Ishida, Surf. Sci. **388**, 71 (1997).
[14] D. Vanderbilt, Phys. Rev. B **41**, 7892 (1990).
[15] For numerical details of the LAPW method for bulk crystals, see, for example, D. J. Singh, *Planewaves, Pseudopotentials, and the LAPW Method* (Kluwer Academic, Norwell, 1994).
[16] J. E. Inglesfield and G. A. Benesh, Phys. Rev. B **37**, 6682 (1988).
[17] S. Crampin, J. B. A. N. van Hoof, M. Nekovee, and J. E. Inglesfield, J. Phys.: Condens. Matter **4**, 1475 (1992); S. Crampin, M. Nekovee, J. B. A. N. van Hoof, and J. E. Inglesfield, Surf. Sci. **287/88**, 732 (1993).
[18] J. B. A. N. van Hoof, thesis, Catholic University of Nijmegen, 1997.
[19] For a bulk crystal with N_a atoms in a unit cell, volume Ω should contain N_a atomic layers.
[20] S_c may be chosen as a plane if the MT spheres are small enough. However, this increases the plane-wave part of the numerical work and ruins the advantages of the LAPW basis set.
[21] Given a wave function subject to the boundary condition $G_{S_c}^{-1}$ on S_c, ψ, one integrates the Schrödinger equation through Δ_L. The embedding potential on S, G_S^{-1}, is defined such that it gives logarithmic derivative of ψ on S.
[22] M. Weinert, J. Math. Phys. **22**, 2433 (1981).
[23] D. D. Koelling and B. N. Harmon, J. Phys. C **10**, 3107 (1977).
[24] S. Blügel, thesis, RWTH Aachen, 1987.
[25] The prefactor 2 accounts for spin. Although we treat only spin-degenerate systems in the present paper, generalizing the method to spin-polazied systems may be self-explanatory.
[26] S_p should be located to the right of S_c or it may be the same as S_c, so that the charge density calculated from the Green function is physically meaningful in the entire volume to the right of S_p. The potential energy on the substrate side of S_p is assumed to be converged to the bulk value.
[27] D. M. Ceperley and B. I. Alder, Phys. Rev. Lett. **45**, 566 (1980). We use the parametrized form due to P. Perdew and A. Zunger, Phys. Rev. B **23**, 5048 (1981).
[28] H. Erschbaumer, A. J. Freeman, W. Fu, and R. Podloucky, Surf. Sci. **243**, 317 (1991).
[29] R. Wu and A. J. Freeman, Phys. Rev. B **45**, 7222 (1992).
[30] G. C. Aers and J. E. Inglesfield, Surf. Sci. **217**, 367 (1989).
[31] S. Clarke, M. Nekovee, P. K. de Boer, and J. E. Inglesfield, J. Phys.: Condens. Matter **10**, 7777 (1998).
[32] H. L. Skriver and N. M. Rosengaard, Phys. Rev. B **45**, 9410 (1992).
[33] M. Heinrichmeier, A. Fleszar, W. Hanke, and A. G. Eguiluz,

Phys. Rev. B **57**, 14 974 (1998).
[34] V. Pallassana, M. Neurock, L. B. Hansen, B. Hammer, and J. K. Norskov, Phys. Rev. B **60**, 6146 (2000).
[35] R. Fischer, S. Scuppler, N. Fischer, Th. Fauster, and W. Steinmann, Phys. Rev. Lett. **70**, 654 (1993).
[36] A. Schäfer, I. L. Shumay, M. Wiets, M. Weinelt, Th. Fauster, E. V. Chulkov, V. M. Silkin, and P. M. Echenique, Phys. Rev. B **61**, 13 150 (2000).
[37] The $\overline{\Gamma}$-$\overline{K}$ line is parallel to the direction connecting two nearest-neighbor atoms in the (111) plane.
[38] S. D. Kevan and R. H. Gayloard, Phys. Rev. B **36**, 5809 (1987).
[39] M. Nekovee, S. Crampin, and J. E. Inglesfield, Phys. Rev. Lett. **70**, 3099 (1993).
[40] S. G. Louie, Phys. Rev. Lett. **40**, 1525 (1978).
[41] S. L. Hulbert, P. D. Johnson, and M. Weinert, Phys. Rev. B **35**, 3670 (1985).
[42] P. J. Feibelman, Phys. Rev. B **26**, 5347 (1982).